

Precession cycles of the El Niño/Southern oscillation-like system controlled by Pacific upper-ocean stratification

Shuai Zhang ^{1,2}, Zhoufei Yu³, Xun Gong ^{4,5,6}, Yue Wang ⁷, Fengming Chang ^{2,6}✉, Gerrit Lohmman ⁵, Yiquan Qi¹ & Tiegang Li^{6,8}✉

Modern observations have presented linkages between subsurface waters of the western Pacific warm pool and both El Niño/Southern Oscillation-related and extratropic-controlled upper-ocean stratification on interannual timescales. Moreover, studies have showed that such controls may operate on orbital cycles, although the details remain unclear. Here we present paired temperature and salinity reconstructions for the surface and thermocline waters in the central western Pacific warm pool over the past 360,000 years, as well as transit modeling results from an Earth system model. Our results show that variations in subsurface temperature and salinity in the western Pacific warm pool have consistently correlated with the shallow meridional overturning cell over the past four glacial-interglacial cycles, and they vary on eccentricity and precession cycles. The shallow meridional overturning cell regulates subsurface waters of the western Pacific warm pool by changing subtropical surface water density and thus equatorial upper-ocean stratification, acting as an El Niño/Southern Oscillation-like process in the precession band. Therefore, the western Pacific warm pool is critical in connecting the austral shallow meridional overturning cell to the Earth's climate system on orbital timescales.

¹Hohai University, Nanjing 210098, China. ²Key Laboratory of Marine Geology and Environment, Institute of Oceanology, Chinese Academy of Sciences, Qingdao 266071, China. ³Nanjing Institute of Geology and Palaeontology, Chinese Academy of Sciences, Nanjing 210008, China. ⁴Hubei Key Laboratory of Marine Geological Resources, China University of Geosciences, Wuhan 430074, China. ⁵Alfred Wegener Institute, Helmholtz Centre for Polar and Marine Research, Bussestrasse. 24, 27570 Bremerhaven, Germany. ⁶Qingdao National Laboratory for Marine Science and Technology, Qingdao 266237, China. ⁷State Key Laboratory of Marine Geology, Tongji University, Shanghai 200092, China. ⁸Key Laboratory of Marine Sedimentology and Environmental Geology, First Institute of Oceanography, MNR, Qingdao 266061, China. ✉email: chfm@qdio.ac.cn; tgli@fio.org.cn

As the greatest source of water vapor and heat on our planet, the western Pacific warm pool (WPWP) plays an important role in the global climate system¹. Modern observations show that the thermocline depth of the WPWP is closely associated with the El Niño/Southern Oscillation (ENSO) evolution² and large-scale changes in extratropical atmospheric circulation¹. In turn, subsurface waters of the western equatorial Pacific (WEP) originate from the subduction of southern Pacific subtropical waters^{3–8}, presenting extratropical control mainly through oceanic tunnels⁹. Therefore, historical records of subsurface waters could provide clues on the past ENSO-like process and the linkage of extratropical climate change to the tropical Pacific¹⁰.

However, sparse and limited paleoceanographic reconstructions have presented diverse histories of subsurface waters in the WPWP on orbital timescales. Two precession-dominated subsurface seawater temperature (subT) records off southern Sumatra¹¹ and Mindanao Island¹² in the far western part of the WPWP were controlled by local monsoon-induced oceanic upwelling processes responding to local summer precessional insolation changes¹¹. Another newly published subT record from the WEP showed a dominant half-precession cycle under bihemispheric influences¹³. A subT record off Papua New Guinea demonstrated clear obliquity cycles since 110 ka, with a warming subT caused by weakened subtropical gyre circulation due to high obliquity¹⁴. Overall, most existing records of subsurface waters of the WPWP have focused on either the last glacial period¹⁰ or regions far from the center of the WPWP^{12,14} and have shown nonuniform information.

Here, we present new paired 360,000-year temperature and salinity records of subsurface water from the thermocline-dwelling planktonic foraminifera species *Neogloboquadrina dutertrei* in the central WPWP (core KX97322-4 in Fig. 1) combined with our previously published sea surface temperature (SST) and salinity (SSS) records from the mixed-layer species *Globigerinoides ruber*¹⁵, enabling further investigation of the orbital-scale upper ocean thermal/salinity structures of the WPWP and their linkage to the southern extratropical oceans and ENSO-like processes over the last four glacial–interglacial cycles.

Results and discussion

Subsurface temperatures and salinities in the central WPWP over the past 360,000 years. Multiple plankton tows have demonstrated that the apparent calcification depth of *N. dutertrei* is 130 m on average off Papua New Guinea¹⁶ and 140–150 m in the eastern part of the WPWP within the upper thermocline¹⁷. Rongstad et al.¹⁸ suggested that the *N. dutertrei* distribution depth in the WEP has a mean of 150 m because the much deeper mixed layer and lower productivity allow warm water and light to penetrate deeper depths in the ocean. Thus, a water depth of 150 m is adopted as the calcification depth of *N. dutertrei* for relative simulation experiments in this study.

The shell Mg/Ca record of *N. dutertrei* fluctuates between 1.2 and 2.6 mmol mol⁻¹ (Supplementary Fig. 1b), corresponding to subT variations between 18.2 and 26.0 °C since 360 ka (Fig. 2b), which is reasonable in terms of the temperature tolerance (15–32 °C) of *N. dutertrei*¹⁹. The average core-top Mg/Ca-derived subT of 23.0 ± 1.1 °C also conforms to modern observations²⁰ at the calcification depth (~150 m) of *N. dutertrei* (Fig. 1). Furthermore, the difference in Mg/Ca of *G. ruber* between the Holocene and Last Glacial Maximum is ~1.1 mmol mol⁻¹ (Supplementary Fig. 1a), comparable to the other relatively high sedimentation rate records (1.1–1.3 mmol mol⁻¹) in the WEP²¹, implying that our temperature signals from core KX97322-4 are not considerably dampened by the effect of bioturbation.

As shown in Fig. 2, the amplitude of subT (~8 °C) is much larger than the range of SST (25.5–30.5 °C) from *G. ruber* over the past 360 kyr (Fig. 2a, b) and exhibits 100-kyr eccentricity and 23 (19)-kyr precession signals (Fig. 2i). In contrast, the SST record of core KX97322-4 is dominated by 100- and 30-kyr cycles, followed by notable 42- and 23-kyr signals (Fig. 2i). This discrepancy suggests different controls on the SST and subT in the central WPWP. Here, orbital-scale SST variations are forced by both local signals (i.e., low-latitude insolation) and global background climate signals (i.e., ice sheets, greenhouse gas concentrations)²². However, subsurface waters in the WEP primarily record low-latitude signals because of their austral origin via the shallow meridional overturning cell (SMOC)^{3,23}. Although the boreal subtropical gyre could also influence the equatorial thermocline

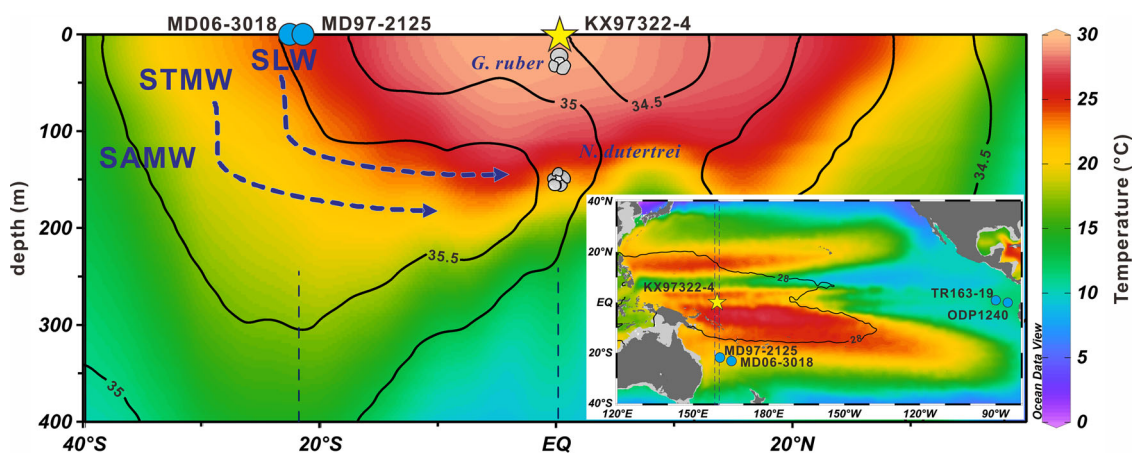


Fig. 1 Core location of KX97322-4 and the distributions of modern temperature and salinity in the equatorial Pacific. The main figure shows temperature (color shading) and salinity (black contour) profiles from 40°S to 40°N along 160°E for 0–400 m water depth. Dashed arrows indicate Subtropical Lower Water (SLW), Subtropical Mode Water (STMW), and Subantarctic Mode Water (SAMW). The inset map shows the modern temperature distribution at 150 m water depth (color shading) based on the World Ocean Atlas 2013 dataset²⁰ using Ocean Data View software²⁵. The dashed 28 °C SST isotherm indicates the extent of the western Pacific warm pool (WPWP). The locations of core KX97322-4 (00°02'S, 159°15'E) from this study and previously published cores MD06-3018 (23°00'S, 166°09'E)²⁸ and MD97-2125 (22°34'S, 161°44'E)²⁷ from the southwestern Pacific and TR163-19 (2°15.5'N, 90°57.1'W)⁶⁷ and ODP 1240 (0°01.3'N, 86°27.8'W)⁵⁵ from the eastern equatorial Pacific (EEP) are shown.

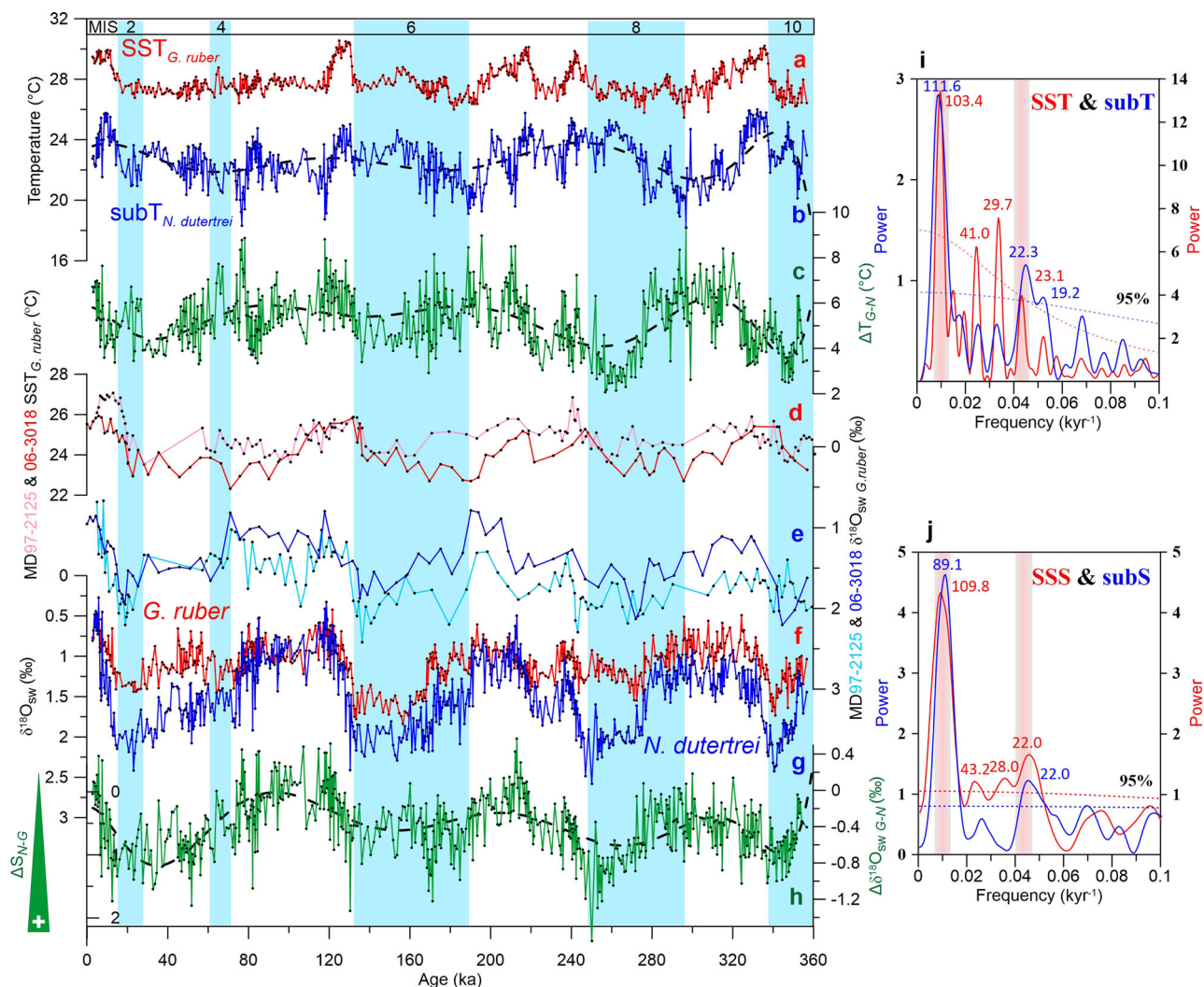


Fig. 2 Variations in surface and subsurface temperatures and $\delta^{18}O_{sw}$ of core KX97322-4 from this study and previously published surface temperature and $\delta^{18}O_{sw}$ records from the southwestern Pacific over the last 360 kyr. **a** Mg/Ca-SST of *G. ruber*; **b** Mg/Ca-subT of *N. dutertrei*; **c** the vertical temperature difference between SST and subT (ΔT_{G-N}); **d** *G. ruber* Mg/Ca-SST of cores MD97-2125 (ref. 27) (pink) and MD06-3018 (ref. 28) (red); **e** $\delta^{18}O_{sw}$ records of *G. ruber* of MD97-2125²⁷ (sky blue) and MD06-3018²⁸ (blue); **f** surface $\delta^{18}O_{sw}$ record from *G. ruber*; **g** subsurface $\delta^{18}O_{sw}$ record from *N. dutertrei*; **h** the salinity difference between subsurface and surface water (ΔS_{N-G}); shaded blue bars indicate glacial intervals and dashed gray curves indicate polynomial fitting of glacial-interglacial cycles; **i** spectral analysis of SST and subT of core KX97322-4; **j** spectral analysis of SSS and subS; dashed curves represent the 95% confidence level. Shaded bars represent the 100-kyr and 23-kyr signals. All data are shown in Supplementary Data 1.

through the western boundary current, it is not discussed here due to its very small contribution attributed to the blocking effect of the Intertropical Convergence Zone (ITCZ)^{8,24}.

The subsurface seawater $\delta^{18}O$ ($\delta^{18}O_{sw}$) deciphered from *N. dutertrei* shares similar features with the surface $\delta^{18}O_{sw}$ in terms of prominent glacial-interglacial variations, although the amplitudes of the subsurface $\delta^{18}O_{sw}$ (average of 2.31‰) are much larger than those of the surface $\delta^{18}O_{sw}$ (average of 1.42‰) (Fig. 2f, g). Furthermore, the average core-top SSS and subsurface seawater salinity (subS) calculated based on $\delta^{18}O_{sw-iv}$ values (see “Methods”) are 35.15 ± 0.22 and 35.18 ± 0.32 (Supplementary Fig. 1e, f), respectively, similar to the in situ salinities of this region at 25 m (34.78) and 150 m (35.10)²⁵ depths. The spectral analyses show that subS exhibits 100- and 23 (19)-kyr signals (Fig. 2j), while SSS exhibits other cycles similar to SST.

Connection between WPWP subsurface waters and the subtropical southern Pacific Ocean. The fluctuations in subT and

subS dominate the variations in ΔT_{G-N} ($SST_{G. ruber} - subT_{N. dutertrei}$) and ΔS_{N-G} ($subS_{N. dutertrei} - SSS_{G. ruber}$), highlighting the prominent roles of subsurface waters in the WPWP on the upper water column structure. Modern observation^{3,4,8} and modeling studies⁵⁻⁷ support that the more saline subsurface water in the modern WEP mainly originates from the subduction of eastern^{6,7} and western^{4,7} south Pacific subtropical waters transported by the SMOC (Fig. 1). Based on an analogy to modern climate and some simulations on orbital-scale^{10,13,26}, changes in the southern extratropical Pacific may account for the large subT and subS variations in the WPWP over the past 360 kyr on orbital timescales.

To identify the orbital-scale extratropical control on the WPWP, we compared our subsurface temperature and $\delta^{18}O_{sw}$ records with published surface temperature and $\delta^{18}O_{sw}$ records from sites MD97-2125 (ref. 27) and MD06-3018 (ref. 28) in the southwestern Pacific. $\delta^{18}O_{sw}$ represents the salinity signals as a passive tracer for the SMOC⁵. The two selected cores are located near the northern edge of the subtropical subduction region in the southwestern Pacific²⁹ and on the route of the SMOC⁴

(Fig. 1), possessing the only available surface water records suitable for comparison. Additionally, we simulated the subT variation (150 m) at our core site as well as the SST variations at two main subduction zones in the southeastern Pacific (20°00'S, 120°00'E) and southwestern Pacific (23°00'S, 166°00'W) over the past 300 kyr (Supplementary Fig. 2) using a community Earth system model (CESM). Here, we present the simulated temperatures in October because subduction is stronger in austral late winter³⁰. Our results show that the variations in subT of core KX97322-4 are quite similar to those in the *G. ruber* Mg/Ca-based SST (~22–27 °C) from sites MD97-2125 (ref. 27) and MD06-3018 (ref. 28) (Fig. 2b, d), although the SST from the southern subtropics exhibited only modest precession cycles²⁸, probably due to their low resolution and/or other complex factors influencing the surface water in that region^{27,28}. However, the simulated results reveal that the SSTs of the two main subduction regions are dominated by precession cycles and exhibit almost synchronous variations with our core over the past 300 kyr (Supplementary Fig. 2). Moreover, there are coherent patterns and similar amplitudes between the *N. dutertrei* $\delta^{18}\text{O}_{\text{sw}}$ record of KX97322-4 and the *G. ruber* $\delta^{18}\text{O}_{\text{sw}}$ records from MD97-2125 and MD06-3018 over the last 360 kyr (Fig. 2e, g). Overall, the results reinforce that the subT and subS signals in the WPWP probably propagated from the subtropical surface to the tropical subsurface through the lower branch of the SMOC.

We also characterize the temperatures and $\delta^{18}\text{O}_{\text{sw-iv}}$ -calculated salinities from cores KX97322-4, MD06-3018, and MD97-2125 in glacial (precession maximum) and interglacial (precession minimum) T–S plots (Fig. 3). The data generally fall between the 23.5 and 24.5 kg m^{-3} isopycnals, and we conclude that the subtropical surface water subducted along isopycnal lines to the equatorial subsurface and consistently influenced the variations in equatorial waters over the last 360 kyr. Additionally, the source of waters that were ventilated in the WPWP included the Subantarctic Mode Water, Subtropical Mode Water, and Subtropical Lower Water³¹ (Fig. 1). These waters passed mainly through the interior channel³² (with perhaps a small part through the western boundary) and mixed with the waters along the route before reaching the equatorial subsurface^{4,31}. Based on the predominant range of the water densities (23.5–24.5 kg m^{-3}) (Fig. 3), we argue that the Subtropical Lower Water (with a density between 24.4 and 24.8 kg m^{-3}) and Subtropical Mode Water (with a density between 24.5 and 25.8 kg m^{-3})³¹ are the primary source waters contributing to the subsurface waters around our core site.

Connection between the WPWP subsurface waters and ENSO-like processes in the precession band. Modern observations demonstrate a strong linkage between $\Delta T_{25-150\text{m}}$ (vertical temperature difference between 25 and 150 m water depth) at site KX97322-4 and the Niño 3.4 index, with a smaller (4.27 ± 1.27 °C) $\Delta T_{25-150\text{m}}$ during a La Niña event and larger (8.15 ± 1.25 °C) $\Delta T_{25-150\text{m}}$ during an El Niño event (Supplementary Fig. 3b) at decadal timescales, which is controlled by the deeper (shallower) thermocline and warmer (cooler) subsurface temperature at the core site, while seawater temperature at 25 m depth changes little (Supplementary Fig. 3b). Since the changes in downcore foraminiferal Mg/Ca-derived ΔT_{G-N} (corresponds to $\Delta T_{25-150\text{m}}$) can be applied to reflect the orbital-scale variations in the depth of the thermocline assuming a constant calcification depth of foraminifera³³, a lower (higher) ΔT_{G-N} represents a deeper (shallower) thermocline and thus weaker (stronger) upper-ocean stratification. After the background glacial–interglacial (GIG) climate signal (dashed gray line in Fig. 2c) is removed, we compare the GIG-detrended ΔT_{G-N} data

(Fig. 4e) of core KX97322-4 with the CESM³⁴ simulated Niño 3 SST of December–January–February (DJF) (Fig. 4i) since 300 ka, and the SST of DJF could sufficiently reflect the changes in paleo-ENSO in the precession band³⁵. Our results show a high positive correlation between the GIG-detrended ΔT_{G-N} of core KX97322-4 and the model-simulated Niño 3 DJF SST in the precession band (Fig. 4e, i). The minimum (maximum) ΔT_{G-N} and lower (higher) Niño 3 SST both indicate a La Niña (El Niño)-like state, in accordance with the modern observed relationship³⁶ (Supplementary Fig. 3b), corresponding to warmer subT (Fig. 4d and Supplementary Fig. 3b) during La Niña (and La Niña-like) conditions and vice versa, which is also supported by our simulated subT result (150 m depth) over the past 300 kyr (Fig. 4c). Moreover, cross-spectrum analyses show high correlations among GIG-detrended subT, ΔT_{G-N} , and ΔS_{N-G} of our core and simulated subT data and Niño 3 SST (Supplementary Fig. 4) in the precession band.

In addition to the temperatures, modern seawater salinities of upper water in the study area also respond to ENSO activity. The $\Delta S_{150-25\text{m}}$ (salinity difference between 150 and 25 m water depth) at site KX97322-4 decreased (increased) during La Niña (El Niño) periods on decadal timescales, ascribed to the increased (decreased) SSS, while $S_{150\text{m}}$ remained nearly stable (Supplementary Fig. 3a). An in situ study showed that the SSS at our core site decreased during El Niño events owing to zonal salt advection and net freshwater flux³⁷. However, in the precession band, the GIG-detrended $\delta^{18}\text{O}_{\text{sw}}$ difference between subsurface and surface $\delta^{18}\text{O}_{\text{sw}}$ values ($\Delta\delta^{18}\text{O}_{\text{sw}}$) deduced from *N. dutertrei* and *G. ruber* behaved oppositely from the modern $\Delta S_{150-25\text{m}}$, showing increased ΔS during La Niña-like states (Fig. 4f, i), which probably resulted from the more saline subsurface water sourced from the southern Pacific, implying that the SMOC-influenced variations in subS contributed more than the precipitation-induced SSS changes at KX97322-4 site in the precession band. At the precession minimum (P_{min}), enhanced evaporation during the austral winter led to increased salinity in the subtropical surface water³⁸, thereby reinforcing subduction and propagating equatorward.

In addition, the hydrological changes in the Indo-Pacific warm pool also respond to ITCZ and monsoon variations, which also have precession cycles^{39,40}. However, the ITCZ mainly works on the surface water cycle (i.e., SSS) north of the equator²⁴ and does not have a potent effect on austral tropical-subtropical interactions. Long-term precipitation records in the central WPWP were more influenced by obliquity than by precession-paced ITCZ and associated Australian summer monsoon variations⁴⁰. Coupled with the thick mixed layer in the central WPWP prohibiting vertical exchange with surface water³, we argue that the subsurface water at our core site is mainly influenced by the subduction of extratropical surface water by the SMOC.

Linkage of WEP subsurface water to global climate in the precession band. In the modern climate, the subtropical gyre has a substantial influence on the ENSO process^{6,7}. On longer timescales, the subtropical gyre may also regulate ENSO-like variations in the tropics and further influence global climate change. A numerical simulation has shown that the modulation of the meridional radiation gradient related to changes in the Earth's obliquity leads to modification of the subtropical gyre⁴¹. In addition, a subT record off Papua New Guinea demonstrated an obliquity cycle with subT warming caused by diminished subduction of relatively cool waters by the weakened subtropical gyre circulation during high obliquity¹⁴. The different signals from ours might be due to the different information documented by different core locations. Another subT record in the WEP

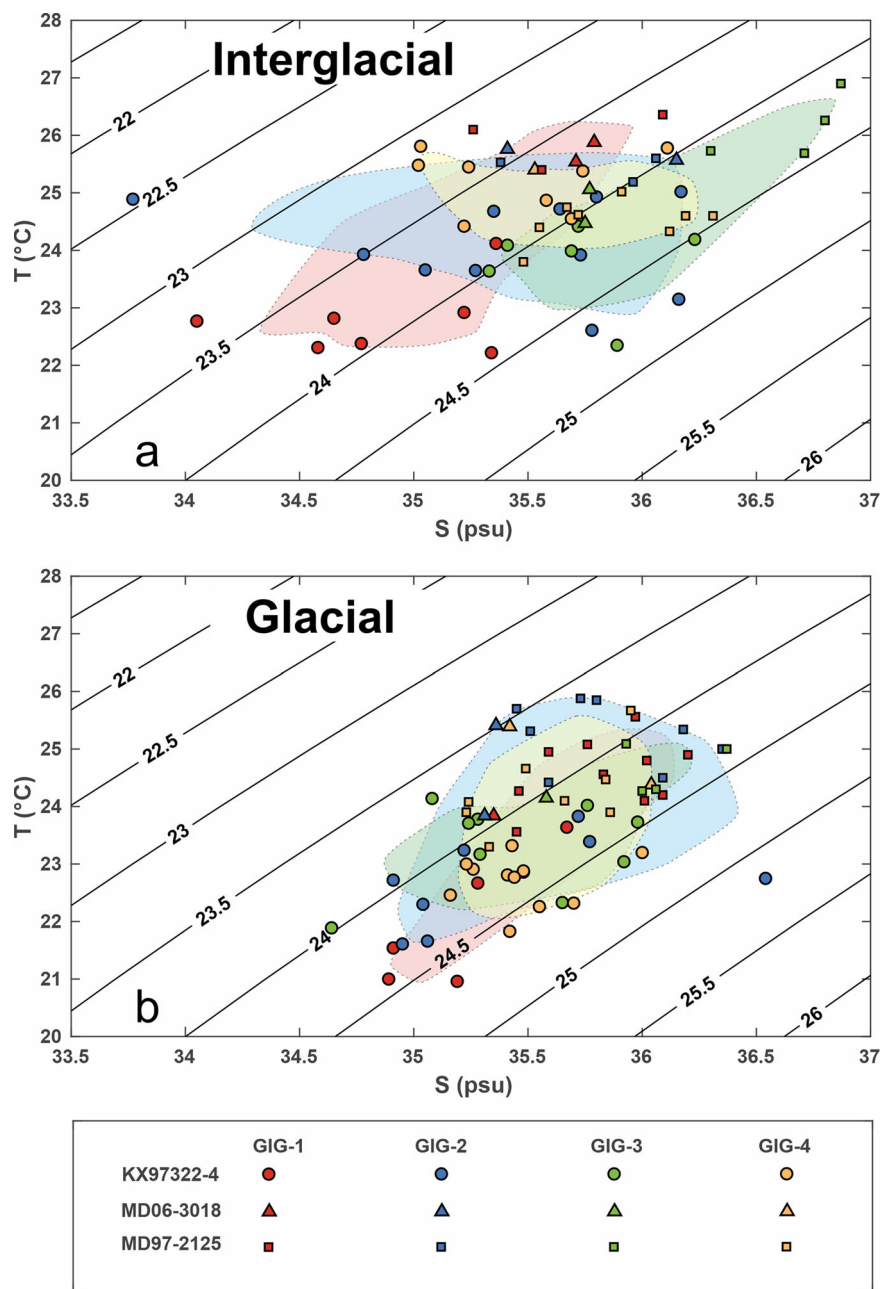


Fig. 3 T-S plot from the southwestern Pacific to the western equatorial Pacific. a Interglacial periods and **b** glacial periods. Glacial-interglacial (GIG)-1, GIG-2, GIG-3, and GIG-4 represent marine isotope stage (MIS) 1/2, MIS 5/6, MIS 7/8, and MIS 9/10, respectively. The four interglacials are defined as 0–5, 125–130, 240–243, and 333–337 kyr in accordance with the periods of precession maxima, and the four glacials are defined as 19–23, 132–139, 252–256, and 338–343 kyr in accordance with the periods of precession minima. Diagonals represent isopycnal surfaces (kg m^{-3}). The colored shading represents the main distribution range of the water temperature–salinity data at each core site, and the closed contour lines are defined as the median of two boundary points.

exhibited a strong half-precession cycle ascribed to the bihemispheric influences at its location¹³. Our results agree with other numerical studies that have proposed that P_{\min} corresponds to enhanced Hadley circulation caused by the occurrence of aphelion near the boreal summer solstice^{42,43}. Precession-paced solar insolation dominates low-latitude climate change via coupled ocean–atmosphere processes^{44,45}. Precipitation records in the Indo-Pacific warm pool generally display dominant precession cycles, as well as productivity variations in the equatorial Pacific and Indian oceans, which have been deduced to be controlled by ENSO-like oscillations at the precession band^{46–48}.

The thermal energy of the tropical and subtropical Pacific is primarily obtained from local insolation⁴⁴. The local insolation at 23°S reaches its maximum in austral winter, corresponding to the climatic precession minimum (Fig. 4a). On the other hand, the minimum insolation differences between summer and winter at 23°S (Fig. 4b) indicate prolonged summers and warm winters in the Southern Hemisphere at P_{\min} . Both conditions should induce a warm anomaly in subtropical surface waters. This scenario is further supported by the simulated result showing the temperature and salinity differences between P_{\min} and P_{\max} (precession maximum) (Fig. 5a), the meridional cross-section in the WPWP

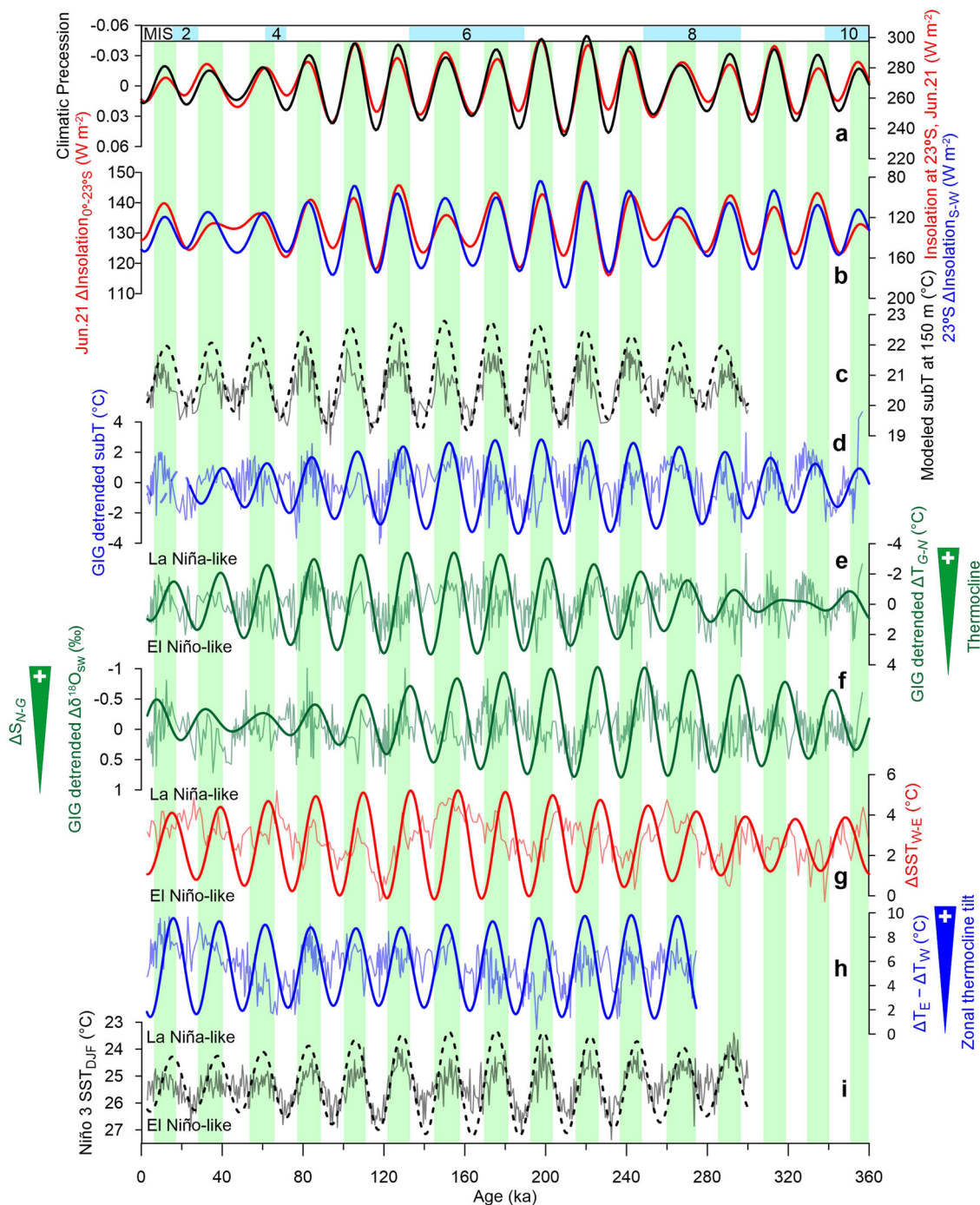


Fig. 4 Comparisons of the upper water column in the central WPWP with the isolation and ENSO-like processes in the precession band. **a** Climatic precession and insolation at 23°S on June 21; **b** insolation difference between 0° and 23°S, as well as between the austral summer and winter; **c** CESM-simulated ocean temperature at 150 m water depth in October at the core site of KX97322-4; **d** glacial-interglacial (GIG) detrended subT from *N. dutertrei* Mg/Ca from this study; **e** GIG-detrended vertical ΔT_{G-N} and **f** ΔS_{N-G} from this study; **g** SST difference between the WEP (core KX97322-4¹⁵) and EEP (core TR163–19 (ref. 67)); **h** comparison of the thermocline depth between the western equatorial (KX97322-4) and eastern equatorial Pacific (ODP 1240 (ref. 55)); the original age model of ODP 1240 was tuned to LR04 for consistency using the Match 2.3.1 software⁵⁷; **i** CESM-simulated Niño3 SST of DJF. The bold curves in **c–i** are the corresponding bandpass filters in the precession band. Upper blue bars indicate glacial intervals, and green bars indicate the periods when precession is less than zero. All data are shown in Supplementary Data 1.

show that a warm and salty anomaly could be traced from the subsurface in the WPWP to its austral source during P_{\min} . In line with the modeling results for the early Holocene (P_{\min}), warm subtropical water heats the region of Subantarctic Mode Water formation, and this warm anomaly is then transported to the tropical subsurface⁴⁹, determined by local austral late winter insolation forcing²⁶.

In addition, the largest insolation gradients between the equator and 23°S occur in the austral winter at P_{\min} ⁵⁰ (Fig. 4b), strengthening the Hadley circulation and intensifying the SMOC by enhancing the surface wind strength (Fig. 5c) and then reinforcing the transfer of warm and salty subtropical water to the equatorial subsurface through isopycnals (Fig. 5b). Furthermore, the enhanced ΔS at P_{\min} expedites surface warming by preventing

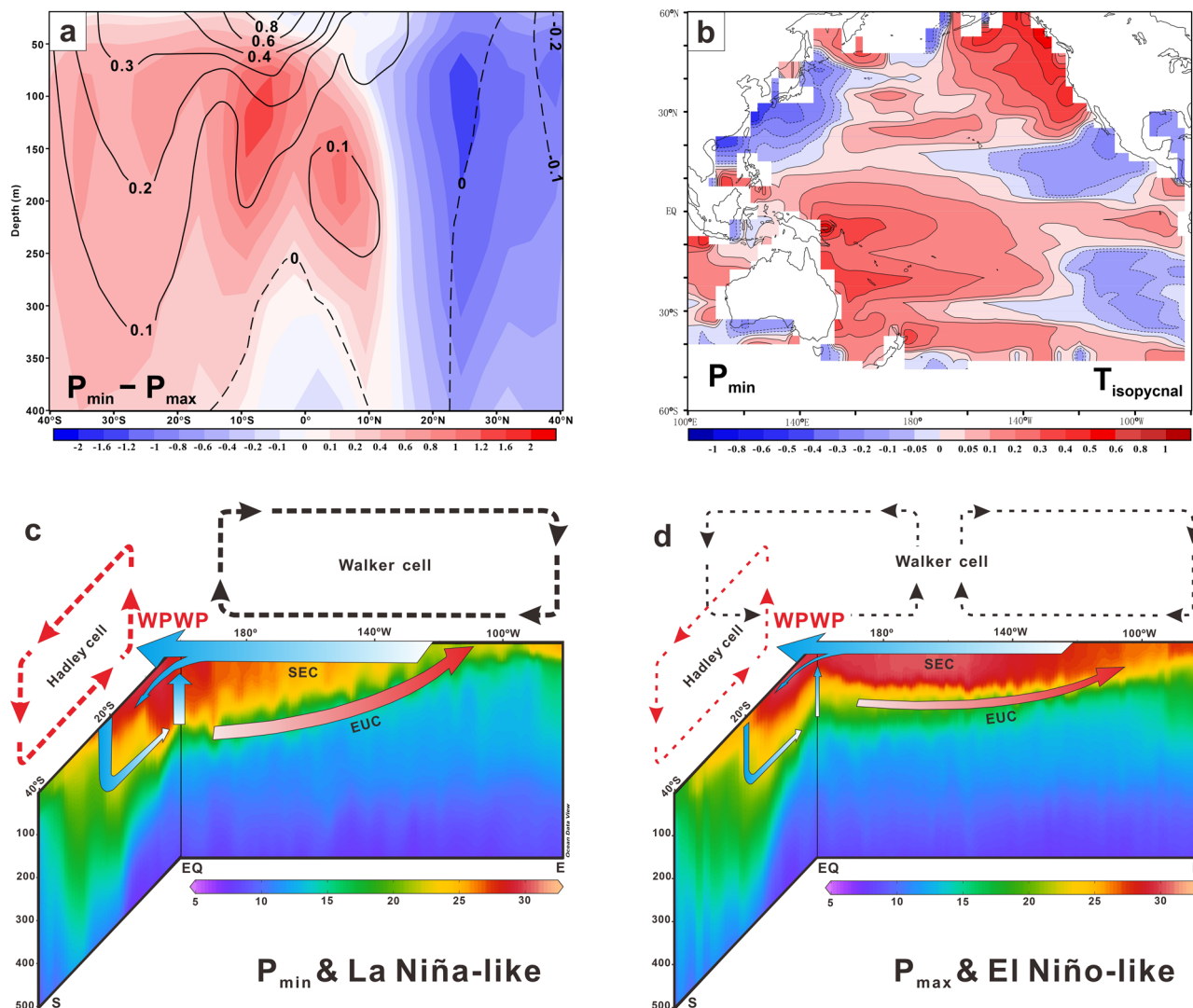


Fig. 5 Thermal state and hypothetical meridional and zonal ocean-atmospheric circulation in the Pacific under precession minimum (P_{min}) and maximum (P_{max}) conditions. **a** Cross-section of CESM-simulated annual mean temperature (color shading, °C) and salinity (contour lines) differences between precession minimum and precession maximum in the WPWP along 160°E; **b** composite difference (°C) of temperature along the 24-25 σ isopycnal surface during P_{min} relative to the 300-kyr climatological mean from CESM simulation; **c** and **d** show the Pacific ocean-atmospheric circulation during P_{min} and P_{max} , respectively. The ENSO-like settings refer to the La Niña event in 2010 (**c**) and the El Niño event in 2015 (**d**), which were collected and made freely available by the International Argo Program and the national programs that contributed to it (<http://www.argo.ucsd.edu>, <http://argo.jcommops.org>). SEC and EUC represent the southern equatorial current and equatorial undercurrent, respectively. Color shading represents water temperature (°C), and the thickness of lines represents the strength of circulations.

downward heat transfer through the thermal barrier effect of a relatively shallow halocline³, causing heat storage in the WEP¹⁰. This process enhances the SST difference between the WEP and eastern equatorial Pacific (EEP) (Fig. 4g) and leads to a much deeper thermocline in the WEP than in the EEP (Fig. 4h, i), promoting a prevailing La Niña-like state (Supplementary Fig. 5a, b). Conversely, P_{max} is dominated by an El Niño-like state (Supplementary Fig. 5c, d). Then, the heated WEP again delivers heat to the subtropical surface through the western boundary current, accomplishing positive feedback. Moreover, WEP warming strengthens the poleward Hadley circulation⁵¹ and encourages more heat to be transferred to high latitudes, thus accelerating the melting of sea ice⁵² and continental ice sheets through atmospheric bridges⁵³. The associated shoaling of the thermocline in the EEP during a La Niña-like state additionally facilitates CO₂ release into the atmosphere⁵⁴. Phase analysis demonstrates that the peak subT in the WPWP is almost in phase with the minimum climatic

precession ($-8.1 \pm 9.1^\circ$) and precedes the peak western equatorial SST ($38.2 \pm 1.0^\circ$), as well as the ENSO-related SST ($101.3 \pm 24.7^\circ$) and thermocline gradient between the WEP and EEP ($94.1 \pm 11.5^\circ$) in the precession band (Supplementary Fig. 6), emphasizing the pivotal role of subsurface waters in the WPWP.

It is worth mentioning that the last four deglaciations are invariably accompanied by a La Niña-like state (Fig. 4) in this study, which is consistent with the reconstructed EEP upwelling intensity⁵⁵ and equatorial Pacific Ocean productivity records⁴⁸. During deglaciations, as insolation increases, low-latitude warming is reinforced by interactions between the equatorial and Southern Hemisphere subtropical regions. The orbital configuration of an obliquity maximum and a precession minimum would accelerate the melting of high-latitude glaciers. Weaker stratification in the equatorial Pacific and sea ice retreat would also induce a greater release of CO₂ to the atmosphere, providing positive feedback to global warming.

Concluding remarks. Our paleoceanographic and modeling results demonstrate that the subsurface temperature and salinity variations in the WPWP over the last 360,000 years are governed by precession-paced insolation that modulated subtropical temperature signals and SMOC variations. As an intermediary between the equatorial and Southern Hemisphere subtropical regions, the subsurface waters in the WPWP superimpose precession-driven subtropical climate variations on the equatorial region, generating a strong influence on ENSO-like processes. During precession minimum (deglaciation) phases, warming of the equatorial subsurface and a shoaling halocline amplify the WPWP warming, inducing a La Niña-like state, and the shoaled thermocline in the EEP would promote increased degassing of CO₂ to the atmosphere, thus accelerating global warming.

Methods

Core KX97322-4 (00°01.73'S, 159°14.66'E, 2362 m) was retrieved from the Ontong Java Plateau in the central WPWP using a giant piston corer on the *Science-1* vessel during the Warm Pool Subject Cruise executed in 2008. The sedimentation rate is 0.39–4.95 cm kyr⁻¹ (Supplementary Fig. 1j), with an average time resolution of 0.57 kyr cm⁻¹.

Age model. The age model was established based on downcore stable oxygen isotope measurements on the benthic foraminifer *Cibicides wuellerstorfi* (>500 μm)¹⁵ correlated with the reference benthic stack LR04 (ref. 56) using Match 2.3.1 software⁵⁷, combined with five accelerator mass spectrometry radiocarbon (¹⁴C) dates on the planktonic foraminifer *Trilobatus sacculifer* (with a sac) (350–500 μm) measured at the National Ocean Sciences Accelerator Mass Spectrometry facility, Woods Hole Oceanographic Institution, USA (Supplementary Fig. 1g, h).

SubT and subS calculations. Approximately 30 tests of *N. dutertrei* (300–355 μm) were picked and crushed and then split into two parts for Mg/Ca and δ¹⁸O analyses for each sample. Samples for Mg/Ca analysis were cleaned following the treatment procedures without a reductive step⁵⁸ because the core was located far from the continent¹⁵. Mg/Ca ratios were analyzed by inductively coupled plasma-optical emission spectrometry (ICP-OES, Thermo Fisher, iCAP6300 radial) at the Institute of Oceanology, Chinese Academy of Sciences with an analytical precision of 0.44% (1σ, relative standard deviation). We chose the calibration equation that was established for *N. dutertrei* from the WPWP with an average standard error of 0.5 °C¹⁶ to calculate subT as follows:

$$\text{Mg/Ca}(\text{mmol mol}^{-1}) = 0.21 \exp[0.097 \times \text{subT}(\text{°C})] \quad (1)$$

To better compare with the Mg/Ca ratio of *G. ruber* from our published work on the same core¹⁵, we also recalculated the SST using the equation for *G. ruber* developed by Hollstein et al.¹⁶ as follows:

$$\text{Mg/Ca}(\text{mmol mol}^{-1}) = 0.26 \exp[0.097 \times \text{SST}(\text{°C})] \quad (2)$$

The Fe/Ca, Al/Ca, and Mn/Ca analyses indicated no substantial contamination (Supplementary Figs. 8 and 9). In addition, we measured the test weights of *G. ruber* and *N. dutertrei* to assess the dissolution effect on Mg/Ca values since Termination II (Supplementary Figs. 10 and 11). Moreover, the influence of salinity on the Mg/Ca ratio of the foraminiferal shell can be ignored in the WPWP¹⁶.

The tests for δ¹⁸O measurements were bathed in 3–6% H₂O₂ for 30 min followed by a 30 s sonication and rinsed with acetone and ultrapure water. Then, the δ¹⁸O of *N. dutertrei* was measured on a GV IsoPrime mass spectrometer at IOCAS calibrated to the Vienna Pee Dee Belemnite via the NBS18 carbonate standard, with an analytical precision of 0.06‰ (1σ). Then, the subsurface δ¹⁸O_{sw} value was calculated with the equation as follows:

$$\delta^{18}\text{O}_{\text{sw}}(\text{SMOW}) = (T_{\text{Mg/Ca}} - 10.5 + 6.58 \times \delta^{18}\text{O})/6.58 + 0.27 \quad (3)$$

which established for *N. dutertrei* obtained from the Indo-Pacific warm pool based on plankton tow and surface sediment samples and laboratory culture results⁵⁹. Subsurface salinity values were calculated by the relationship as follows:

$$\delta^{18}\text{O}_{\text{sw-iv}}(\text{SMOW}) = 0.74 \times \text{Salinity} - 25.4 (R^2 = 0.9) \quad (4)$$

which generated for WEP intermediate water with an uncertainty of the absolute salinity better than ±0.69 (ref. 60). We selected this equation to avoid the potential influence of variable surface waters in other equations, and δ¹⁸O_{sw-iv} is the ice-volume corrected δ¹⁸O_{sw} value using the mean ocean water δ¹⁸O value⁶¹.

Spectral and phase analysis. We used redfit spectral analysis with Past 3.20 software⁶² to investigate the potential mechanism for subsurface temperature and salinity variations over the past 360 kyr. We also used Redfit-X 1.1 (ref. 63) to analyze the phase relations between the precession index and other proxies.

Detrended fluctuation and filtering analysis. We used a ninth-order polynomial fit to obtain the glacial-interglacial trend of the proxies and then subtracted the trend from the original data to obtain localized signals. We also used fast Fourier transform filters to perform bandpass filtering of the proxy data with a cutoff frequency between 0.04 and 0.046 to emphasize cyclic variations in the 23-kyr precession band.

Numerical simulation. To model tropical and subtropical temperature variations, we used the CESM with T31_gx3v7 resolution (3.75° × 3.75° resolution for the atmosphere and nominal 3° resolution for the ocean) to extract the Niño 3 SST in DJF and the upper water temperature of the equatorial and austral subtropical regions. As a spin-up, the CESM was run for 200 model years under fixed orbital parameters of 300 kyr BP, with all other boundary conditions set to their values in 1950 AD. Then, the model was integrated for 3000 model years with the transient orbital insolation forcing of the past 300,000 years, in which orbital parameters were advanced by 100 years at the end of each model year⁶⁴. This transient experiment was called CESM_orb³⁴, and its outputs for the last 3000 model years were used in our analysis. This coarse-resolution model can reproduce the modern variability in the tropical ENSO, including its two different spatial types (eastern Pacific-type and central Pacific-type), in a realistic manner due to its improved convection scheme³⁵ (Supplementary Fig. 7). It is reasonable to select this model for our analysis in view of the successful application of coarse-resolution models to paleo-ENSO changes under orbital forcing^{13,65,66}.

Data availability

All data in the paper are present in the paper and the supplementary materials. All the data named as “Sable oxygen isotope and Mg/Ca ratios of planktonic foraminifera from KX97322-4 (KX22-4)” can also be obtained from PANGAEA (<https://www.pangaea.de/>) or NOAA (<https://www.nccei.noaa.gov>) with the reference ID: UKRLJ3 or from the authors.

Code availability

Codes for CESM (version 1.0.4) are publicly available at <https://www.cesm.ucar.edu/models/cesm1.0/>.

Received: 23 March 2021; Accepted: 28 October 2021;

Published online: 22 November 2021

References

- Cane, M. A. Climate change: a role for the tropical Pacific. *Science* **282**, 59–61 (1998).
- Webster, P. J. & Palmer, T. N. The past and the future of El Niño. *Nature* **390**, 562–564 (1997).
- Lindstrom, E. et al. The Western Equatorial Pacific Ocean Circulation Study. *Nature* **330**, 533–537 (1987).
- Ganachaud, A. et al. The Southwest Pacific Ocean circulation and climate experiment (SPICE). *J. Geophys. Res. Oceans* **119**, 7660–7686 (2014).
- Shin, S.-I. & Liu, Z. Response of the equatorial thermocline to extratropical buoyancy forcing. *J. Phys. Oceanogr.* **30**, 2883–2905 (2000).
- Giese, B. S., Urizar, S. C. & Fučkar, N. S. Southern hemisphere origins of the 1976 climate shift. *Geophys. Res. Lett.* **29**, 1-1–1-4 (2002).
- Luo, J.-J. et al. South Pacific origin of the decadal ENSO-like variation as simulated by a coupled GCM. *Geophys. Res. Lett.* **30**, 2250 (2003).
- Johnson, G. C. & McPhaden, M. J. Interior pycnocline flow from the subtropical to the equatorial Pacific Ocean. *J. Phys. Oceanogr.* **29**, 3073–3089 (1999).
- Liu, Z. & Yang, H. Extratropical control of tropical climate, the atmospheric bridge and oceanic tunnel. *Geophys. Res. Lett.* **30**, 1230 (2003).
- Dang, H. et al. Pacific warm pool subsurface heat sequestration modulated Walker circulation and ENSO activity during the Holocene. *Sci. Adv.* **6**, eabc0402 (2020).
- Wang, X. et al. Precession-paced thermocline water temperature changes in response to upwelling conditions off southern Sumatra over the past 300,000 years. *Quat. Sci. Rev.* **192**, 123–134 (2018).
- Bolliet, T. et al. Mindanao Dome variability over the last 160 kyr: episodic glacial cooling of the West Pacific Warm Pool. *Paleoceanography* **26**, PA1208 (2011).
- Jian, Z. et al. Half-precessional cycle of thermocline temperature in the western equatorial Pacific and its bihemispheric dynamics. *Proc. Natl Acad. Sci. USA*, 201915510 (2020).
- Hollstein, M. et al. Variations in Western Pacific Warm Pool surface and thermocline conditions over the past 110,000 years: forcing mechanisms and implications for the glacial Walker circulation. *Quat. Sci. Rev.* **201**, 429–445 (2018).

15. Zhang, S. et al. Correspondence between the ENSO-like state and glacial-interglacial condition during the past 360 kyr. *Chin. J. Oceanol. Limnol.* **35**, 1018–1031 (2017).
16. Hollstein, M. et al. Stable oxygen isotopes and Mg/Ca in planktic foraminifera from modern surface sediments of the Western Pacific Warm Pool: Implications for thermocline reconstructions. *Paleoceanography* **32**, 1174–1194 (2017).
17. Rippert, N. et al. Constraining foraminiferal calcification depths in the western Pacific warm pool. *Mar. Micropaleontol.* **128**, 14–27 (2016).
18. Rongstad, B. L. et al. Investigating ENSO-related temperature variability in Equatorial Pacific core-Tops using Mg/Ca in individual planktic foraminifera. *Paleoceanogr. Paleoclimatol.* **35**, e2019PA003774 (2020).
19. Bijma, J., Faber, W. W. & Hemleben, C. Temperature and salinity limits for growth and survival of some planktonic foraminifera in laboratory cultures. *J. Foraminiferal Res.* **20**, 95–116 (1990).
20. Locarnini, R. A. et al. World Ocean Atlas 2013, Volume 1: Temperature. in *NOAA Atlas NESDIS 73*, 40 (ed. Levitus, S., technical ed. Mishonov, A.) (2013).
21. de Garidel-Thoron, T. et al. A multiproxy assessment of the western equatorial Pacific hydrography during the last 30 kyr. *Paleoceanography* **22**, PA3204 (2007).
22. Tachikawa, K., Timmermann, A., Vidal, L., Sonzogni, C. & Timm, O. E. Southern Hemisphere orbital forcing and its effects on CO₂ and tropical Pacific climate. *Clim. Past Discuss.* **9**, 1869–1900 (2013).
23. Qu, T. & Gao, S. Resurfacing of South Pacific tropical easter in the Equatorial Pacific and its variability associated with ENSO. *J. Phys. Oceanogr.* **47**, 1095–1106 (2017).
24. Lu, P. & McCreary, J. P. Influence of the ITCZ on the flow of thermocline water from the subtropical to the equatorial Pacific Ocean. *J. Phys. Oceanogr.* **25**, 3076–3088 (1995).
25. Schlitzer, R. Ocean Data View 4, <http://odv.awi.de> (2015).
26. Liu, Z., Brady, E. & Lynch-Stieglitz, J. Global ocean response to orbital forcing in the Holocene. *Paleoceanography* **18**, 1041 (2003).
27. Tachikawa, K., Vidal, L., Sonzogni, C. & Bard, E. Glacial/interglacial sea surface temperature changes in the Southwest Pacific ocean over the past 360 ka. *Quat. Sci. Rev.* **28**, 1160–1170 (2009).
28. Russon, T. et al. The mid-Pleistocene transition in the subtropical southwest Pacific. *Paleoceanography* **26**, PA1211 (2011).
29. O’Kane, T. J., Monselesan, D. P. & Maes, C. On the stability and spatiotemporal variance distribution of salinity in the upper ocean. *J. Geophys. Res. Oceans* **121**, 4128–4148 (2016).
30. Stommel, H. Determination of water mass properties of water pumped down from the Ekman layer to the geostrophic flow below. *Proc. Natl Acad. Sci. USA* **76**, 3051–3055 (1979).
31. Sokolov, S. & Rintoul, S. Circulation and water masses of the southwest Pacific: WOCE Section P11, Papua New Guinea to Tasmania. *J. Mar. Res.* **58**, 223–268 (2000).
32. Lee, T. & Fukumori, I. Interannual-to-decadal variations of tropical–subtropical exchange in the Pacific Ocean: boundary versus interior pycnocline transports. *J. Clim.* **16**, 4022–4042 (2003).
33. Farmer, E. C., Kaplan, A., de Menocal, P. B. & Lynch-Stieglitz, J. Corroborating ecological depth preferences of planktonic foraminifera in the tropical Atlantic with the stable oxygen isotope ratios of core top specimens. *Paleoceanography* **22**, PA3205 (2007).
34. Wang, Y., Jian, Z., Zhao, P., Chen, J. & Xiao, D. Precessional forced evolution of the Indian Ocean dipole. *J. Geophys. Res. Oceans* **120**, 3747–3760 (2015).
35. Wang, Y. et al. Precessional forced zonal triple-pole anomalies in the tropical Pacific annual cycle. *J. Clim.* **32**, 7369–7402 (2019).
36. Carton, J. A. & Giese, B. S. A reanalysis of ocean climate using Simple Ocean Data Assimilation (SODA). *Mon. Weather Rev.* **136**, 2999–3017 (2008).
37. Delcroix, T. & Picaut, J. Zonal displacement of the western equatorial Pacific “fresh pool”. *J. Geophys. Res. Oceans* **103**, 1087–1098 (1998).
38. Lamy, F. et al. Precession modulation of the South Pacific westerly wind belt over the past million years. *Proc. Natl Acad. Sci. USA* **116**, 23455–23460 (2019).
39. Zhang, P. et al. Indo-Pacific hydroclimate in response to changes of the intertropical convergence zone: discrepancy on precession and obliquity bands over the last 410 kyr. *J. Geophys. Res. Atmos.* **125**, e2019JD032125 (2020).
40. Liu, Y. et al. Obliquity pacing of the western Pacific Intertropical Convergence Zone over the past 282,000 years. *Nat. Commun.* **6**, 1–7 (2015).
41. Lee, S. Y. & Poulsen, C. J. Tropical Pacific climate response to obliquity forcing in the Pleistocene. *Paleoceanography* **20**, PA4010 (2005).
42. Merlis, T. M., Schneider, T., Bordoni, S. & Eisenman, I. Hadley circulation response to orbital precession. Part I: Aquaplanets. *J. Clim.* **26**, 740–753 (2012).
43. Clement, A. C., Seager, R. & Cane, M. A. Orbital controls on the El Niño/Southern oscillation and the tropical climate. *Paleoceanography* **14**, 441–456 (1999).
44. Loutre, M.-F., Paillard, D., Vimeux, F. & Cortijo, E. Does mean annual insolation have the potential to change the climate? *Earth Planet. Sci. Lett.* **221**, 1–14 (2004).
45. Laepple, T. & Lohmann, G. Seasonal cycle as template for climate variability on astronomical timescales. *Paleoceanography* **24**, PA4201 (2009).
46. Dang, H., Jian, Z., Kissel, C. & Bassinot, F. Precessional changes in the western equatorial Pacific Hydroclimate: a 240 kyr marine record from the Halmahera Sea, East Indonesia. *Geochem. Geophys. Geosyst.* **16**, 148–164 (2015).
47. Carolin, S. A. et al. Northern Borneo stalagmite records reveal West Pacific hydroclimate across MIS 5 and 6. *Earth Planet. Sci. Lett.* **439**, 182–193 (2016).
48. Beaufort, L., de Garidel-Thoron, T., Mix, A. C. & Pisias, N. G. ENSO-like forcing on oceanic primary production during the Late Pleistocene. *Science* **293**, 2440–2444 (2001).
49. Kalansky, J., Rosenthal, Y., Herbert, T., Bova, S. & Altabet, M. Southern Ocean contributions to the Eastern Equatorial Pacific heat content during the Holocene. *Earth Planet. Sci. Lett.* **424**, 158–167 (2015).
50. Laskar, J. The chaotic motion of the solar system: a numerical estimate of the size of the chaotic zones. *Icarus* **88**, 266–291 (1990).
51. Wang, C. Atmospheric circulation cells associated with the El Niño–Southern oscillation. *J. Clim.* **15**, 399–419 (2002).
52. Ding, Q. et al. Tropical forcing of the recent rapid Arctic warming in northeastern Canada and Greenland. *Nature* **509**, 209–212 (2014).
53. Rodgers, K. B., Lohmann, G., Lorenz, S., Schneider, R. & Henderson, G. M. A tropical mechanism for Northern Hemisphere deglaciation. *Geochem. Geophys. Geosyst.* **4**, 1046 (2003).
54. Bova, S. C. et al. Links between eastern equatorial Pacific stratification and atmospheric CO₂ rise during the last deglaciation. *Paleoceanography* **30**, 1407–1424 (2015).
55. Pena, L. D., Cacho, I., Ferretti, P. & Hall, M. A. El Niño–Southern Oscillation–like variability during glacial terminations and interlatitudinal teleconnections. *Paleoceanography* **23**, PA3101 (2008).
56. Lisiecki, L. E. & Raymo, M. E. A Pliocene–Pleistocene stack of 57 globally distributed benthic $\delta^{18}\text{O}$ records. *Paleoceanography* **20**, PA1003 (2005).
57. Lisiecki, L. E. & Lisiecki, P. A. Application of dynamic programming to the correlation of paleoclimate records. *Paleoceanography* **17**, 1049 (2002).
58. Barker, S., Greaves, M. & Elderfield, H. A study of cleaning procedures used for foraminiferal Mg/Ca paleothermometry. *Geochem. Geophys. Geosyst.* **4**, 8407 (2003).
59. Bouvier-Soymagnac, Y. & Duplessy, J.-C. Carbon and oxygen isotopic composition of planktonic foraminifera from laboratory culture, plankton tows and recent sediment; implications for the reconstruction of paleoclimatic conditions and of the global carbon cycle. *J. Foraminiferal Res.* **15**, 302–320 (1985).
60. Rosenthal, Y., Linsley, B. K. & Oppo, D. W. Pacific Ocean heat content during the past 10,000 years. *Science* **342**, 617–621 (2013).
61. Spratt, R. M. & Lisiecki, L. E. A Late Pleistocene sea level stack. *Clim. Past* **12**, 1079–1092 (2016).
62. Hammer, Ø., Harper, D. & Ryan, P. PAST–Paeontological Statistics, ver. 1.89. *Palaeontol. Electron.* **4**, 1–9 (2001).
63. Björg Ólafsdóttir, K., Schulz, M. & Mudelsee, M. REDFIT-X: cross-spectral analysis of unevenly spaced paleoclimate time series. *Comput. Geosci.* **91**, 11–18 (2016).
64. Kutzbach, J. E., Liu, X., Liu, Z. & Chen, G. Simulation of the evolutionary response of global summer monsoons to orbital forcing over the past 280,000 years. *Clim. Dyn.* **30**, 567–579 (2008).
65. Lu, Z., Liu, Z., Chen, G. & Guan, J. Prominent precession band variance in ENSO intensity over the last 300,000 years. *Geophys. Res. Lett.* **46**, 9786–9795 (2019).
66. Liu, Z. et al. Evolution and forcing mechanisms of El Niño over the past 21,000 years. *Nature* **515**, 550–553 (2014).
67. Lea, D. W., Pak, D. K. & Spero, H. J. Climate impact of Late Quaternary Equatorial Pacific sea surface temperature variations. *Science* **289**, 1719–1724 (2000).

Acknowledgements

We appreciate the sea-board assistance of cruise KX08-973 and the laboratory assistance of X. Yu, Z. Xiong, H. Wang, and Y. Ding. This study was funded by the Strategic Priority Research Program of the Chinese Academy of Sciences (Grant No. XDB42000000) and by the National Natural Science Foundation of China (Grant Nos. 41830539, 41906058, 41706040, 41606045, and 41976047). It was also supported by the China Postdoctoral Science Foundation (No. 2017M611667), State Key Laboratory of Marine Geology, Tongji University (No. MGK1711), and Open Fund of the Key Laboratory of Marine Geology and Environment, Chinese Academy of Sciences (No. MGE2017KG07). X.G. and G.L. thank the NOPAWAC project of Germany (BMBF Grant No. 03F0785A).

Author contributions

T.L., F.C., and S.Z. designed the study. S.Z. and Z.Y. sampled the core and performed the Mg/Ca and $\delta^{18}\text{O}$ analyses. S.Z., X.G., and Y.W. contributed to the interpretation of the data. Y.W. designed and performed the simulations. S.Z. wrote the manuscript, and Z.Y., X.G., Y.W., F.C., T.L., G.L., and Y.Q. provided comments and revisions.

Competing interests

The authors declare no competing interests.

Additional information

Supplementary information The online version contains supplementary material available at <https://doi.org/10.1038/s43247-021-00305-5>.

Correspondence and requests for materials should be addressed to Fengming Chang or Tiegang Li.

Peer review information *Communications Earth & Environment* thanks the anonymous reviewers for their contribution to the peer review of this work. Primary Handling Editor: Joe Aslin.

Reprints and permission information is available at <http://www.nature.com/reprints>

Publisher's note Springer Nature remains neutral with regard to jurisdictional claims in published maps and institutional affiliations.



Open Access This article is licensed under a Creative Commons Attribution 4.0 International License, which permits use, sharing, adaptation, distribution and reproduction in any medium or format, as long as you give appropriate credit to the original author(s) and the source, provide a link to the Creative Commons license, and indicate if changes were made. The images or other third party material in this article are included in the article's Creative Commons license, unless indicated otherwise in a credit line to the material. If material is not included in the article's Creative Commons license and your intended use is not permitted by statutory regulation or exceeds the permitted use, you will need to obtain permission directly from the copyright holder. To view a copy of this license, visit <http://creativecommons.org/licenses/by/4.0/>.

© The Author(s) 2021